



Critical Parameters and Mechanisms of Chromium Removal from Water by Copper-Based Nanoparticles

Fotini Noli · Argyro Dafnomili ·
Catherine Dendrinou-Samara · Maria Kapnisti ·
Eleni Pavlidou

Received: 4 July 2022 / Accepted: 2 December 2022 / Published online: 20 December 2022
© The Author(s) 2022

Abstract This research aims to explore the chromium removal from water using copper-based nanoparticles. The nanoparticles were synthesized by hydrothermal method and characterized by X-ray diffraction, scanning electron microscopy, infrared spectroscopy, and X-ray photoelectron spectroscopy as well as determination of the specific surface area (S_{BET}) and point of zero charge (PZC). The size and composition of nanoparticles are influenced by the reaction time, organic coating, and oxidizing atmosphere. Sorption experiments were carried out in aqueous solutions as well as simulated drinking water at various initial concentration, time, and temperature. Cu nanoparticles had a significant Cr uptake capacity of $3.4 \text{ mg}\cdot\text{g}^{-1}$ for $C_{\text{in}} 1.0 \text{ mg}\cdot\text{L}^{-1}$ lowering the Cr

concentration below the provisional guideline value of $50 \text{ }\mu\text{g}\cdot\text{L}^{-1}$. Sorption isotherms were fitted to Henry, Langmuir, and Freundlich models, whereas kinetic data were reproduced by different kinetic models. Iodide sorption experiments were carried out to explore the sorption mechanism onto Cu-NPs. Considering the biocompatibility, stability, good uptake capacity, and reusability, Cu nanoparticles could be considered as promising agents for applications in water purification.

Keywords Chromium · Iodide · Copper nanoparticles · Water purification · Sorption · Radiotracers

Supplementary Information The online version contains supplementary material available at <https://doi.org/10.1007/s11270-022-06009-6>.

F. Noli (✉) · A. Dafnomili · C. Dendrinou-Samara
Department of Chemistry, Aristotle University
of Thessaloniki, 54124 Thessaloniki, Greece
e-mail: noli@chem.auth.gr

M. Kapnisti (✉)
Department of Food Science and Technology, International
Hellenic University, P.O. Box 141, 57400 Thessaloniki,
Greece
e-mail: mariakap@ihu.gr

E. Pavlidou
Department of Physics, Aristotle University
of Thessaloniki, 54124 Thessaloniki, Greece

1 Introduction

In all countries, water pollution is a serious concern because people come into contact with heavy and toxic metals, as well as radionuclides, through water. Chromium (III) is an essential micronutrient, and its deficiency may lead to diabetic syndromes, while chromium (VI) is highly toxic and carcinogenic for humans. According to WHO guidelines for drinking water quality, the guideline value of $50 \text{ }\mu\text{g/L}$ is proposed for total chromium [Acharya et al., 2021; Mohamed et al., 2020].

Chromium existence in natural waters is of great concern due to its high chemical toxicity which depends on its oxidation state. Its natural sources in

the environment are the ore deposits, where it is frequently found as chromium-iron minerals. It can be found in large amounts in both soil and plants. It usually appears in the environment as Cr(III), which is less toxic and immobile, but after oxidation, at an alkaline pH, and in the presence of MnO_2 and other chromium-containing minerals, it may appear as Cr(VI), extremely toxic and mobile form that predominates in groundwater. However, apart from its natural origin, chromium is also associated with anthropogenic activities, primarily industrial and chemical units where chromium is used in pigments and dyes, wood preservatives, chrome plating, ore, and petroleum refining. Metal alloys, such as stainless steel, magnetic strips, and protective coatings, are some of the uses of chromium [Des Marias & Costa, 2019; Sharma et al., 2021].

There is extensive literature on the difference between the bioavailability and bioactivity of Cr(III) and Cr(VI) and how its presence in natural waters corresponds to an increased incidence of cancer [Prasad et al., 2021; Sharma et al., 2021]. However, the removal of chromium from water is still a scientific research topic. A wide number of techniques (e.g., precipitation, adsorption, biosorption, photocatalyst, flotation, microbial fuel cell, electrochemical treatment, membrane technology, ion exchange, and reverse osmosis) that have been used for the removal of metals can also be applied to chromium [Jawed et al., 2020]. Furthermore, the most commonly used method is sorption, which involves the use of a variety of natural and synthetic materials and the synergistic reduction of Cr(VI) to less soluble Cr(III) [Farooqi et al., 2021; Kaprara et al., 2013 & 2017; Zhang et al., 2022]. The combination and development of the techniques mentioned above could provide solutions to the problem of Cr mitigation in polluted sites.

Among the various materials used as adsorbents over the years, nanoparticles, due to their small size and therefore their large surface area, have demonstrated very high performance in the removal of metals from wastewater and have been successfully applied in remediation technology [Wadhawana et al., 2020]. However, disadvantages such as nanoparticle agglomeration, which reduces effective surface area and sorption efficiency, as well as synthesis costs, demand additional efforts in developing new materials.

Concerning Cr removal by nanoparticles, many articles are referred on the use of iron-based NPs as adsorbents. For example, Zhu et al., 2018 used nanosheets embellished nano iron for effective removal of chromium (VI). Bampaiti et al., 2013 used zero-valent iron (ZVI) nanoparticles to reduce Cr(VI) to Cr(III), which then precipitates. Based on an electrochemical corrosion reaction mechanism, iron and iron compounds have been shown to be capable of reducing agents for Cr(VI) [Bampaiti et al., 2013; Simeonidis et al., 2015; Zhu et al., 2018]. This mechanism involves Cr(VI) sorption on the sorbent's surface and subsequent reduction to the less soluble and toxic Cr(III), as well as iron oxidation. Recently, various nanoparticles such as chitosan, inorganic NPs, and carbon nanotubes, have been used to sorb hexavalent chromium from groundwater [Abuzalat et al., 2020; Acharya et al., 2021; Bampaiti et al., 2013; Farooqi et al., 2021; Gözetten and Tunç, 2022; Kaprara et al., 2017; Simeonidis et al., 2015]. Copper nanoparticles (Cu-NPs) have also recently been implemented in environmental technology. Up to our knowledge, relatively little is known concerning the application of Cu-NPs, as adsorbents for metal removal [Chandra & Khan, 2020; Zarrabi & Ghasemi-Fasaee, 2021; Khani et al., 2018; Liu, 2012]. Copper as bio essential metal linked to the flexible redox system, combining antimicrobial properties and economical way of elaboration can be a promising material in water purification. Furthermore, copper nanoparticles were permitted by EPA (US Environmental Protection Agency) as an antimicrobial agent.

The use of coated copper-based nanoparticles for Cr sorption from water is demonstrated in this study. Different organic ligands as coating were tested, including tetra ethylene and polyethylene glycol (TEG and PEG), because terminal groups influence aggregation, solubility, and activity of the NPs. Reactions such as reduction and/or hydrolysis take place, resulting in the formation of metallic and/or oxide nanoparticles [Poul et al., 2003]. Increasing the reaction time led to the formation of new oxalates heterogeneous nanoparticles. Sorption experiments were carried out in simulated water regarding the effect of concentration, contact time, and temperature. Furthermore, attempts have been made to explore the sorption procedure using a variety of methods such as XRD, SEM-EDS, FTIR, and XPS, as well as mathematical models.

2 Experimental Part

2.1 Materials

All reagents were analytical grade, and all preparations were made using double distilled water. $\text{Cu}(\text{NO}_3)_2 \cdot 3\text{H}_2\text{O}$, N_2H_4 , tetra ethylene, and polyethylene glycol (TEG and PEG8000) were used for the synthesis of nanoparticles. $\text{K}_2\text{Cr}_2\text{O}_7$ and NaI (Merck pro analysis) were used to prepare the solutions for the sorption experiments.

2.2 Synthesis of Nanoparticles

The copper-based nanoparticles formed in autoclaves under autogenous pressure when copper nitrate was decomposed in the presence of tetra ethylene and polyethylene glycol (TEG and PEG8000) as organic coating. The procedure followed the same protocol of hydrothermal synthesis as described elsewhere [Antonoglou and Dendrinou-Samara, 2021; Gautam et al., 2018; Gkanatsiou et al., 2019]. Different reaction time and temperature gave rise to different products (for Cu/TEG 2 h at 120 °C, for Cu-mix/TEG 14 h at 120 °C, for Cu-ox/PEG 2 h at 120 °C, and for Cu/PEG 2 h at 160 °C, see Table 1). The ratio of precursor to organic coating was 1:1.

For the synthesis, 4.1 mmol (1 g) $\text{Cu}(\text{NO}_3)_2 \cdot 3\text{H}_2\text{O}$ were used dissolved in 10 mL deionized water leading in a blue-colored solution. Then, 4.1 mmol (0.207 g) of $\text{N}_2\text{H}_4 \cdot \text{H}_2\text{O}$ were added dropwise to the solution under vigorous stirring, and the color changed from blue to yellowish, due to the reduction of Cu^{2+} , while 2.1 mL organic coating was added. The solution after stirring was transferred into a 23-mL Teflon-lined stainless steel autoclave and remains for crystallization for 4 h, at 120 °C. Then, the autoclave was cooled naturally to room temperature. After centrifugation at 5000 rpm, the supernatant liquid was discarded, and the formed black-brown precipitate was washed at

least three times with ethanol denatured to remove the excess of ligands and unreacted precursors.

Oxidation of polyols can take place during the synthesis, and according to the reaction temperature and time, different oxidized species and intermediates are formed. When small reaction times are applied, 39 nm copper metal nanoparticles are obtained, while at long reaction times, the excess of TEG and the oxidizing atmosphere led to oxidation of copper and formation of oxalates with final formation of heterogeneous nanoparticles with size 38–45 nm. The oxidation of TEG to oxalate results in $\text{Cu}(\text{C}_2\text{O}_4)$ NPs due to extensive fragmentation of the TEG molecules and especially the ether-type bonds of TEG.

2.3 The Characterization of the Materials

The morphology and microstructure as well as the particle size and constitution of the materials were revealed by SEM–EDS using the JEOL JSM-6390LV electron microscope, respectively. The FTIR spectra were recorded with a Thermo Scientific Nicolet 6700 FTIR spectrometer whereas the powder X-ray diffraction (pXRD) diagrams using the model X'Pert Pro MPDP analytical, Almelo, The Netherlands with Cu $\text{K}\alpha$ ($\lambda=0.154$ nm) radiation and 2θ degrees scanning region 6–80° (step size: 0.04°) with scan speed 0.027°s⁻¹.

The zero-charge point was found out by preparing dilute sorbent suspensions of different pH values and plotting their zeta potentials vs. pH. Zeta potential is used to measure the charge on nanoparticles, and it is defined as the potential of a nanoparticle's shear surface relative to a bulk medium [Gautam et al., 2018]. It was determined in the pH range 1–10, by using Zeta-nanosized (Nano-ZS90) Brookhaven Instruments Zeta Potential Analyzer using Phase Analysis Light Scattering (ZetaPALS), with a viscosity of 890cP and a refractive index for the aqueous phase of 1.330, at 25 °C.

Table 1 The nanoparticles used and their properties

Sample	Composition	Size (nm)	Organic coating
Cu/TEG	Cu	39	TEG (3–4%)
Cu-mix/TEG	$\text{Cu}(\text{C}_2\text{O}_4)/\text{Cu}_2(\text{OH})_3\text{NO}_3$	38–52	TEG (35–40%)
Cu-ox/PEG	Cu-oxidized	16	PEG (16%)
Cu/PEG	Cu	40	PEG8000 (60%)

Nitrogen adsorption–desorption isotherms were taken to investigate the surface properties of the Cu-NPs, using the Thermo Scientific Surfer Analyzer gas adsorption porosimeter at the temperature of liquid nitrogen (77 K) after the samples were preheated and outgassed for 6 h at 378 K. The specific surface area (S_{BET}) was calculated by applying the Brunauer–Emmett–Teller (BET) method. The adsorption capacity in the relative pressure (P/P_0) at 0.95 was used to obtain the total pore volume. Furthermore, X-ray photoelectron spectroscopy (XPS) was applied, at the Kratos Analytical AXIS Ultra^{DL}D system, with aluminum monochromatic X-ray source ($\lambda_{\text{Ka}} = 1.4866 \text{ \AA}$), under high vacuum conditions (10^{-8} torr).

2.4 Sorption Study

For the chromium adsorption experiments, solutions were prepared from the $\text{K}_2\text{Cr}_2\text{O}_7$ stock solution of 500 mg Cr(VI)/L in concentrations of 0.25, 0.5, 1, 2, 5, 8, 10, 12, 15 mg·L⁻¹. The solutions were spiked with a small amount of $\text{K}_2\text{Cr}_2\text{O}_7$ which was ⁵¹Cr-labeled and acted as a radiotracer (E_γ : 321 keV, ⁵¹Cr: $t_{1/2}$: 27.7 days), and their pH was adjusted to 7 with dilute HNO_3 and NaOH solutions [Bampaiti et al., 2013]. A total of 10 mg of adsorbent was combined with 50 mL of the corresponding chromium solution in polypropylene centrifuge tubes for 24 h. Preliminary tests revealed that a 24-h contact time was adequate to achieve equilibrium. The solid phase was separated from the liquid phase after this time with centrifugation at 4000 rpm for 10 min and then filtration through a 0.22- μm membrane filter. Chromium concentration was determined in the liquid phase by gamma-ray spectroscopy (γ -line at 321 keV) with an HPGe detector (CANBERRA, REGe detector, efficiency 20%, energy resolution 2.1 keV for the 1332 keV ⁶⁰Co γ -radiation), which was connected to a computer-based gamma-spectroscopy set-up. Based on the obtained data, Cr removal (mg/g) was calculated, and the corresponding isotherms were constructed.

Sorption experiments were also undertaken in simulated water at the same experimental conditions as described above for Cr aqueous solutions. Although many researchers have reported the effects of possible interfering species (e.g., Fe(III), Mn(II), Na(I), K(I), Cl^- , SO_4^{2-} , NO_3^-) to chromium (VI) in

natural and polluted wastewaters, the simulated natural water, used in this work, contained the common interfering ions and was freshly prepared according to the National Sanitation Foundation (NSF) protocols (Table S1) [Jiang et al., 2019; Mohamed et al., 2020].

Chromium kinetics experiments were conducted at 25 °C (ambient temperature), 40 °C, and 55 °C. A total of 50 mg of the substance was mixed with a 250 mL of 10 mg·L⁻¹ solution. For the determination of their Cr content, samples were obtained at the following times: 0, 60, 240, 360, 480, 960, 1440, 1860, 2400, and 2880 min.

2.5 Iodide Adsorption Experiments

Iodide adsorption experiments were performed to explore the mechanism. The iodide solutions were made from 1000 mg·L⁻¹ NaI solution, at concentrations of 17 and 170 mg·L⁻¹, with the addition of ¹³¹I, radioisotope (in NaI form), which has a half-life of 8.02 days and decays by β -decay to ¹³¹Xe (stable). The equilibrium concentration was determined using gamma-ray spectroscopy on an HPGe detector at 364 keV, which corresponds to the gamma-ray emission of iodine-131.

A mass of 10 mg of adsorbent was mixed for 24 h with a volume of 50 and 10 mL of the respective iodine solutions—at adjusted pH 7—in plastic centrifuge tubes. The solutions were then centrifuged; the liquid phase was taken up to measure the iodine activity.

2.6 Equilibrium and Kinetic Modeling

Equilibrium pH (pH_{eq}) of the supernatant solutions was also measured. All the experimental results were averages of duplicate experiments, with a relative uncertainty of the experimental values of less than 5%. Equation (1) was used to find the amount of sorbed metal, q_e (mg·g⁻¹) combining the initial (C_{init} , mg·L⁻¹) and equilibrium (C_e , mg·L⁻¹) concentrations with the solution volume, V (L) and the mass of the sorbent, m (g)

$$q_e = \frac{C_{\text{init}} - C_e}{m} V \quad (1)$$

Different models were used to fit the sorption data. At the examined temperature, sorption isotherms

show the relationship between the amount of a component sorbed per sorbent mass and the remaining solution concentration after equilibrium. The parameters of the used models give information for the sorption procedure. The correlation coefficient, R^2 , was used to assess the fit [Lima et al., 2015].

The Henry isotherm is regarded as the simplest adsorption isotherm model and describes a linear relationship between adsorption and equilibrium concentration where constant, K_D , represents the interaction of a single molecule with all the atoms in the solid adsorbent [Prasetyo et al., 2018]. The model is expressed by Eq. (2):

$$q_e = K_D C_e \tag{2}$$

The Langmuir model is written as Eq. (3) [Langmuir, 1916]. It is based on the premise that the sorption energy is constant across all sites and that a saturated sorbate monolayer forms on the sorbent surface, predicting a theoretical monolayer sorption capacity (q_{max} , $\text{mg}\cdot\text{g}^{-1}$),

$$q_e = \frac{q_{max} K_L C_e}{K_L C_e + 1} V \tag{3}$$

where K_L gives the Langmuir equilibrium constant, which is related to the sorption energy ($\text{L}\cdot\text{mg}^{-1}$). By linearizing Eq. (3), K_L and q_{max} are determined from the intercept and slope of the linear plots of C_e/q_e vs. C_e .

The Freundlich model is shown in Eq. (4). It is an empirical equation and describes heterogeneous energy distribution on the sorbent surface [Freundlich, 1906]

$$q_e = K_F C_e^{1/n} \tag{4}$$

where K_F denotes the Freundlich constant, which is related to sorption capacity. $1/n$ that ranges between 0 and 1 is a measure of surface heterogeneity: the closer it is to zero, the more heterogeneous the surface. Plotting $\log q_e$ vs. $\log C_e$ yielded K_F (intercept) and $1/n$ (slope).

Pseudo-first and pseudo-second order as well as Elovich and intraparticle diffusion (IPD) models were used to fit kinetic data [Liu & Liu, 2008]. Equation (5) represents the pseudo-first-order model and is commonly used to describe sorption from a liquid phase:

$$\frac{dq_t}{dt} = k_1 (q_e - q_t) \tag{5}$$

The linear form (6) is used to calculate the pseudo-first-order rate constant (min^{-1}), k_1 , from the plot $\ln(q_e - q_t)$ vs. t . q_t and q_e ($\text{mg}\cdot\text{g}^{-1}$) are the amount of the sorbed metal at time t and at equilibrium, respectively.

$$\ln(q_e - q_t) = k_1 t + \ln q_e \tag{6}$$

Sorption may involve the exchange or sharing of electrons between the sorbate and the sorbent, according to the pseudo-second-order model. The model is written as (7)

$$\frac{dq_t}{dt} = k_2 (q_e - q_t)^2 \tag{7}$$

The rate constant, k_2 ($\text{g}\cdot\text{mg}^{-1}\cdot\text{min}^{-1}$) of the process, and the equilibrium capacity, q_e ($\text{mg}\cdot\text{g}^{-1}$) in the above experimental settings, are calculated using the linear form (8) from the slope and intercept of plot t/q_t versus t .

$$\frac{t}{qt} = \frac{1}{q_2 q_e^2} + \frac{1}{q_e} t \tag{8}$$

Elovich Eq. (9) has been successfully applied to describe the chemical adsorption process and is appropriate for systems with heterogeneous adsorbing surfaces. It has been shown to cover a wide variety of slow adsorption rates [Gözeten and Tunç, 2022; Vagheti et al., 2009].

$$\left(\frac{dq_t}{dt}\right) = \alpha e^{-\beta q_t} \tag{9}$$

α ($\text{mg}\cdot\text{g}^{-1}\cdot\text{min}^{-1}$) denotes the initial sorption rate constant, and β ($\text{g}\cdot\text{mg}^{-1}$) is proportional to the extent of surface covering and the activation energy of chemisorption. The model parameters are calculated from the linear form (Eq. 10)

$$q_t = \frac{1}{\beta} \ln(\alpha\beta) + \frac{1}{\beta} \ln t \tag{10}$$

The effect of mass transfer resistance on Cr(VI) binding to the Cu-NPs was investigated using the intraparticle diffusion model proposed by Weber and Morris (Eq. 11) [Vagheti et al., 2009]:

$$q_t = k_{int} t^{1/2} + C \quad (11)$$

k_{int} ($\text{mg}\cdot\text{g}^{-1}\cdot\text{min}^{-0.5}$) is the IPD rate constant, and C indicates the thickness of boundary layer. If the plot of q_t vs. $t^{1/2}$ passes through the origin, then intraparticle diffusion is the rate-determining step.

The thermodynamic parameters, which are enthalpy (ΔH^0), entropy (ΔS^0), and Gibbs free energy (ΔG^0), were derived from equilibrium constants, K , using Eqs. (12) and (13) [Lima et al., 2015].

$$\Delta G^0 = -RT \ln K \quad (12)$$

$$\Delta G^0 = \Delta H^0 - T \Delta S^0 \quad (13)$$

Equations (12) and (13) are used to form Van't Hoff Eq. (14). The value of ΔH^0 was determined by the slope of the $\log K$ vs. $1/T$ plot.

$$\ln K = \frac{\Delta S^0}{R} - \frac{\Delta H^0}{RT} \quad (14)$$

2.7 Regeneration Experiments

The regeneration of the adsorbent was performed through acid treatment (H_2SO_4 1 M) and EDTA, 1 M respectively. The loaded nanoparticles (50 mg), after interaction with Cr solution (metal concentration $15 \text{ mg}\cdot\text{L}^{-1}$), were contacted with 50 mL of H_2SO_4 or EDTA solutions. After shaking the mixtures for 2 h, the liquid phase was taken up for chromium concentration measurement, while the solid phase, after washing with distilled water, was reused in the 2nd sorption–desorption cycle.

3 Results and Discussion

3.1 Materials Properties and Characterization

The investigated sorbents and their characteristics concerning their type, the NPs size, and the percentage of the organic coating in the final product are presented in Table 1.

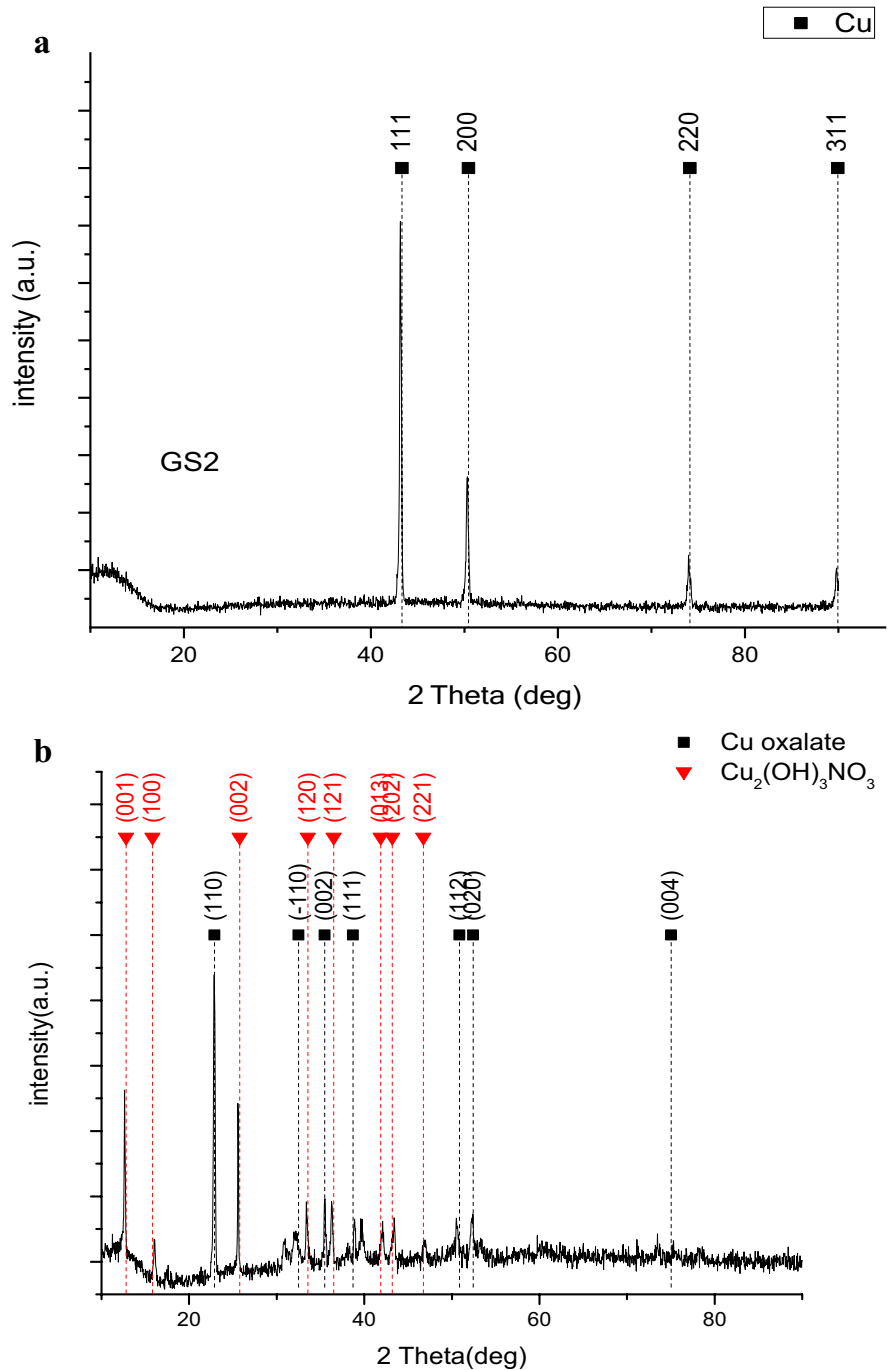
XRD was used to confirm the materials' composition, as shown in Fig. 1, which shows the XRD patterns for Cu/TEG and Cu-mix/TEG, whereas the characterization of Cu-ox/PEG and Cu/PEG materials is presented in previous work (Giannousi et al.,

2014, 2016). According to the ICDD (International Center for Diffraction Data) database, it appears that for the Cu/TEG nanoparticles, a phase of elemental copper was identified, with characteristic reflections (111), (200), (220), and (311), reference card: pdf. 04–0836. The nanoparticle size was calculated according to the Scherrer equation and found to be 39 nm. For Cu-mix/TEG nanoparticles, a copper oxalate phase appears, with characteristic reflections of (110), (-110), (002), (111), (112), (020), and (004), according to the reference card: pdf: 21–0297. A second phase, copper nitrate hydroxide, also occurs, with reflections (001), (100), (002), (120), (121), (013), (202), and (221), according to reference card: pdf: 15–0014.

The presence of functional groups (and organic coating) was demonstrated by the FTIR spectra (Fig. S1) and will be discussed later. In general, in the case of the Cu/TEG, the characteristic peaks of methylene groups ($-\text{CH}_2$) are obvious at 2920 and 2850 cm^{-1} and the one of hydrogen bonds ($\text{H}\dots\text{H}$) at 1626 cm^{-1} . The peak near 1380 cm^{-1} is attributed to the vibration of the C-O bond of ethers. In the case of the Cu-mix/TEG, the following peaks appear: 1436 , 1317 , 1046 , and 817 cm^{-1} due to the presence of nitrates ($-\text{ONO}_2$), 1375 cm^{-1} due to hydroxy nitrates, 1623 cm^{-1} the attenuated vibration of the carboxylic bond C-O of the acids, and an acute vibration at 512 cm^{-1} due to the Cu-OCCO bond [Gkanatsiou et al., 2019].

pH_{pzc} is essential for identifying the optimal pH for adsorption testing and comprehending the mechanisms of adsorption. It defines a precise pH value below which adsorbents' net surface charge is regarded to be positive. Figure 2, illustrating the pH–zeta potential diagrams of the materials Cu/TEG and Cu-mix/TEG, shows that the pH_{pzc} for Cu/TEG is 8.2. When solution pH is below the pH_{pzc} , the Cu/TEG surface is positively charged due to protonation of the surface functional groups, becoming readily available to the negatively charged HCrO_4^- , via electrostatic interaction. The positive value of the surface charge decreases as the pH rises, until it is zero. When the pH of the solution exceeds pH_{pzc} , the CrO_4^{2-} compete with the OH^- ions, which provide an electro-repulsive force that interferes with the adsorbent's binding sites, preventing Cr(VI) adsorption. However, electrostatic attraction is not completely inhibited at pH values slightly above pH_{pzc} . Cu-mix/

Fig. 1 XRD patterns of the samples **a** Cu/TEG and **b** Cu-mix/TEG



TEG exhibits a negative surface charge throughout the pH scale, but never reaches the zero point. As the pH of the solution rises, the absolute value of the negative charge rises as well. Since the negative charges on the surface for the electrostatic attraction of the anions predominate, it can be concluded that there is

a different mechanism for the removal of chromates. However, electrostatic attraction cannot be completely ruled out [Mortazavian et al., 2018].

The nitrogen adsorption–desorption isotherms for Cu/TEG and Cu-mix/TEG are depicted in Fig. 3. Using the BET equation, the surface area

Fig. 2 Zeta potential vs. pH plots for the sorbents Cu/TEG and Cu-mix/TEG

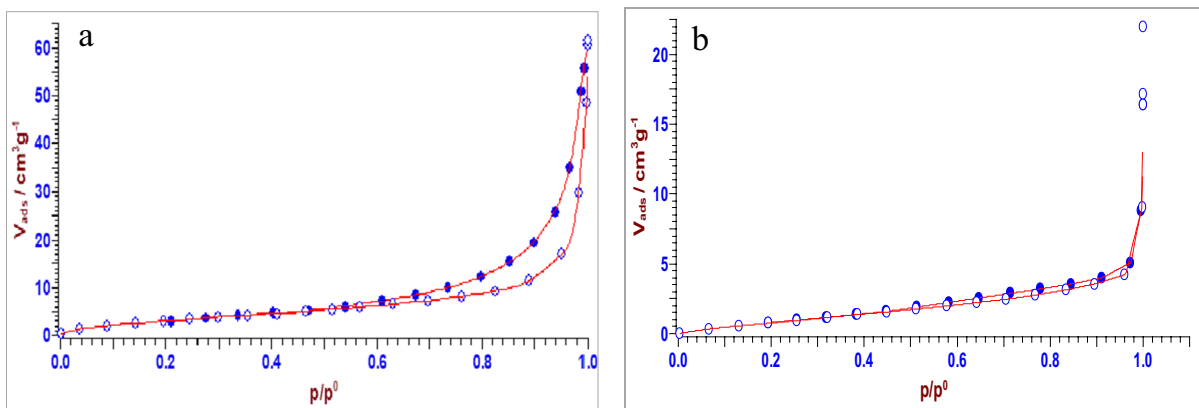
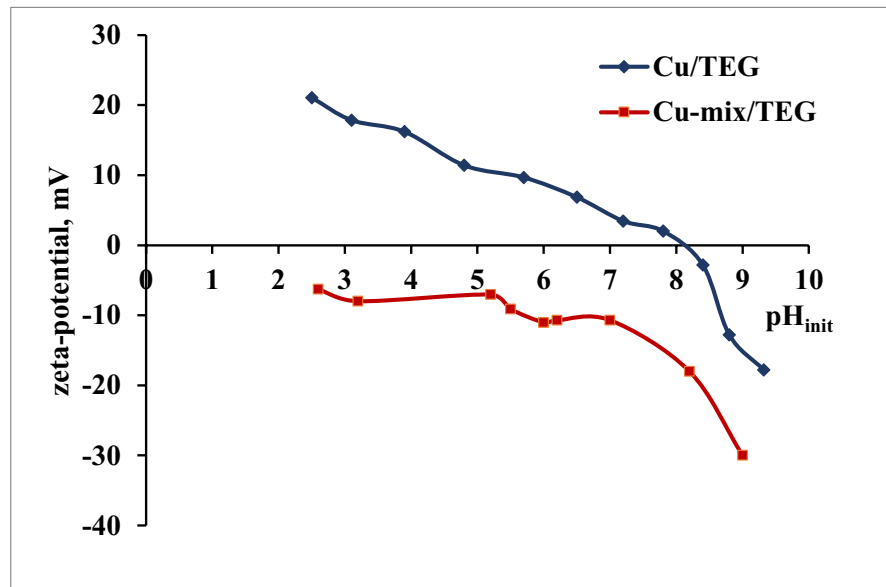


Fig. 3 N_2 adsorption–desorption isotherms at 77 K for **a** Cu/TEG **b** Cu-mix/TEG

was determined in the relative pressure range $P/P_0=0.05–0.30$. Cu/TEG has three to four times greater surface area and pore capacity than Cu-mix/TEG, which is normally considered advantageous for Cr(VI) adsorption [Zhang et al., 2022]. Cu/TEG exhibits a Type IV isotherm, as described by IUPAC [Sing, 1985]. The pore volume is $0.026 \text{ cm}^3\cdot\text{g}^{-1}$, and the calculated specific surface area was found to be $13.67 \text{ m}^2\cdot\text{g}^{-1}$ for Cu/TEG. There is a small uptake step at a relative pressure (P/P_0) under 0.01, indicating the presence of some micropores. At P/P_0 below 0.4, an overlap is observed between the isotherms of adsorption and desorption, showing

the microporous filling. A distinct hysteresis loop appears at $0.5 < P/P_0 < 1$, which results from the phenomenon of the capillary condensation, and indicates the existence of some mesopores, which may form as a result of gaps between the organic coating and the NPs.

Cu-mix/TEG has a Type II isotherm and is a non-porous substance having a specific surface area of $4.15 \text{ m}^2\cdot\text{g}^{-1}$ and a pore volume of $0.0064 \text{ cm}^3\cdot\text{g}^{-1}$.

Hexavalent chromium, Cr(VI), can exist in various ionic forms in the aqueous phase, depending on the pH of the solution. In the pH 2 to 6, Cr(VI) exists as HCrO_4^- and $\text{Cr}_2\text{O}_7^{2-}$, in aqueous solutions,

while in pH greater than 6, its existence form is CrO_4^{2-} [Sahoo et al., 2021; Yi et al., 2017].

The speciation diagram of chromium ion species based on concentration and pH, constructed by computer code MEDUSA [Puigdomènech, 1983], is given in Fig. S2. CrO_4^{2-} is the dominating species in the pH area under examination.

3.2 Sorption Investigation

3.2.1 Chromium Adsorption Experiments

Adsorption tests were performed with $15 \text{ mg}\cdot\text{L}^{-1}$ aqueous chromium solutions for the five adsorbents Cu/TEG, Cu-mix/TEG, Cu-ox/TEG, and Cu/PEG.

The adsorption capabilities of these materials are depicted in the histogram in Fig. 4; however, only Cu/TEG and Cu-mix/TEG were of special interest because the adsorption capacities of the other two materials were relatively low; therefore, Cu/TEG and Cu-mix/TEG were chosen for further investigation.

Figure 5 shows the adsorption isotherms of chromium from adsorbents Cu/TEG and Cu-mix/TEG, at pH 7 in aqueous solutions and simulation water, respectively. The experiments were performed at ambient temperature, with chromium concentrations ranging from 0.25 to $15 \text{ mg}\cdot\text{L}^{-1}$.

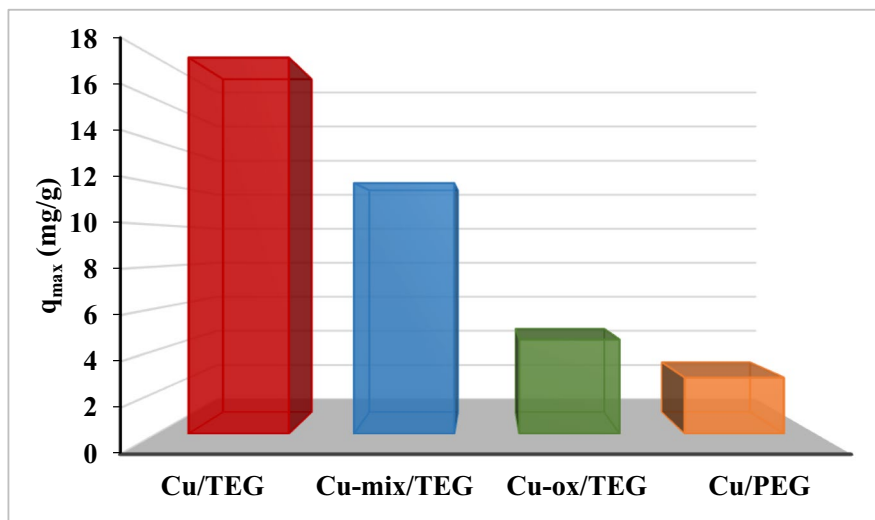
According to the experimental results, at concentrations less than $8 \text{ mg}\cdot\text{L}^{-1}$, both Cu/TEG and Cu-mix/TEG exhibit similar behavior. At higher concentrations, Cu/TEG exhibits higher adsorption

capacity. The pH of the aqueous chromium solutions was measured at the end of the adsorption experiments and after equilibration, and it was observed that both materials at low concentrations (1 to $8 \text{ mg}\cdot\text{L}^{-1}$) caused a slight drop in the pH of the solution. On the other hand, at higher concentrations, they showed an equally small increase in pH.

It was observed that at initial concentrations lower than $1.0 \text{ mg}\cdot\text{L}^{-1}$, the equilibrium concentration of chromium in both aqueous solutions and simulated water was below the permissible limit of $50 \text{ }\mu\text{g}\cdot\text{L}^{-1}$ as it is shown in Fig. 5d. The materials tested in this research exhibited higher capacity for Cr removal (q_{max} : 13.5 – $19.1 \text{ mg}\cdot\text{g}^{-1}$), with respect to other materials referred in the literature and especially for nanoparticles used in water purification [Gupta et al., 2016]. For example, Simeonidis et al. observed Cr removal capacity of $1.8 \text{ mg}\cdot\text{g}^{-1}$ for a residual concentration of $50 \text{ }\mu\text{g}\cdot\text{L}^{-1}$ in natural water, and the observed capacity for the same residual concentration was $3.4 \text{ mg}\cdot\text{g}^{-1}$ [Simeonidis et al., 2015].

Table 2 shows the simulation results with the isothermal equations Langmuir and Freundlich. The Freundlich equation is the best simulation for Cu/TEG nanoparticles suggesting a surface heterogeneity, while the Langmuir equation is the best simulation for Cu-mix/TEG nanoparticles indicating a monomolecular coverage of the surface. For the case of adsorption with water simulated with Cu/TEG nanoparticles, the Freundlich equation again shows the best fit.

Fig. 4 Adsorption tests for $15 \text{ mg}\cdot\text{L}^{-1}$ aqueous chromium solution



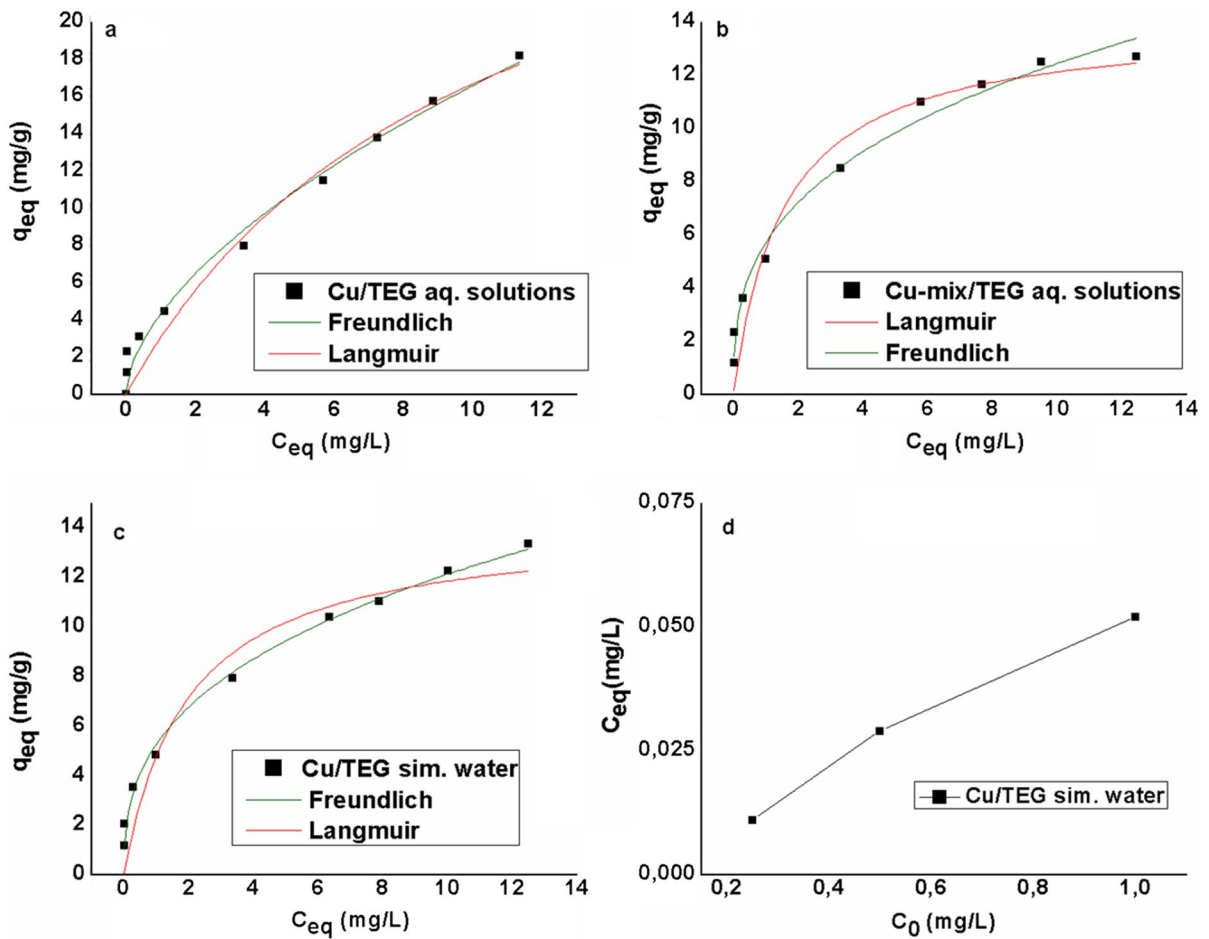


Fig. 5 a–c Chromium adsorption isotherms with Cu/TEG and Cu-mix/TEG nanoparticles in aqueous solution and simulated water (0.25–15 mg·L⁻¹, pH 7) and **d** C_{eq} values in relation to the initial Cr concentration.

3.2.2 Iodide Adsorption Tests

Iodide adsorption studies were carried out in order to better understand and draw conclusions regarding the operating mechanisms of the two materials, Cu/TEG and Cu-mix/TEG. Figure 6 presents the results of the tests carried out in NaI solutions with concentrations of 170 and 17 mg/L and using different adsorbent-to-solution ratios.

The Cu-mix/TEG material has a greater sorption capacity at a concentration of 170 mg/L with an adsorbent-solution ratio of 1:1, whereas the Cu/TEG material has a higher sorption capacity at a ratio of 1:5. When the amount of solution is increased, the Cu/TEG material has a high adsorption capacity due to its wide surface area, leading to the conclusion that

it functions via an adsorption mechanism. Cu-mix/TEG material, on the other hand, operates by an ion exchange mechanism since its adsorption capacity is similar in both amounts, which indicates that it can remove the radioactive isotope only as long as there are free binding sites, regardless of the quantity of metal in the solution. Based on the experimental results, it was proved that the removal of chromium with the Cu-mix/TEG material is based on the ion exchange mechanism, while with the Cu/TEG material mainly on the adsorption mechanism.

3.2.3 Kinetics and Thermodynamic Data

Figure 7 shows the results of kinetic experiments of chromium aqueous solutions of concentration

Table 2 Parameters of the Langmuir and Freundlich isothermal equations

Models	Parameters	Cu/TEG		Cu-mix/TEG
		Aq. solution	Simul. H ₂ O	Aq. solution
Experiment	q_{exp} (mg/g)	18.2	13.4	12.7
Henry	K_D (L/g)	1.88	1.73	1.71
	R^2	0.9955	0.9271	0.8762
Langmuir	K_L (L/mg)	0.85	1.00	0.91
	q_{max} (mg/g)	19.1	13.8	13.5
	R^2	0.7686	0.9637	0.9850
Freundlich	K_F	5.27	5.58	5.96
	1/n	0.385	0.314	0.307
	R^2	0.9872	0.9826	0.9791

10 mg·L⁻¹ at pH 7, with the adsorbent Cu/TEG. The experiments were performed at temperatures of 25, 40, and 55 °C. The times for these experiments reached 48 h as it was observed that there was a long delay in completing the adsorption.

The kinetics of Cr removal from Cu-NPs found to follow the pseudo-second-order model, as shown in Fig. S3, with a straight line in the plot t/q_t versus t for all examined temperatures (25, 40, and 55 °C).

Table 3 shows the corresponding k_2 values and correlation coefficient squared (R^2).

As can be seen in Table 3, pseudo-second-order and Elovich models present high R^2 values. However, there is no good agreement of the experimental adsorption capacity for the 10 mg·L⁻¹ solution with the calculated adsorption capacity from the pseudo-second-order model. Thus, the kinetic data were suitably fitted to the Elovich model. This gives strong evidence that chemical sorption involving sharing or replacing electrons occurs between sorbent and sorbate and confirms the finding of surface heterogeneity due to the Freundlich equation fitting. The rate constants increased as the temperature increased, indicating that diffusion reactions play a significant role in the control of the adsorption process. The rate-controlling step can be explained by the intraparticle diffusion model. The graphs of q_t vs. $t^{1/2}$ were not linear over the whole range, showing that the adsorption was impacted by more than one mechanism. The different natures of the plots may be explained by boundary layer diffusion, which provided the first step, and intraparticle diffusion, which provided the second step [Cheung et al., 2007] (Fig. S4).

The Van't Hoff diagram of $\ln K$ as a function of $1/T$ (Fig. S5) gives a linear line with a coefficient $R^2=0.9884$ and was used to determine enthalpy (ΔH^0), Gibbs free energy (ΔG^0), and entropy (ΔS^0).

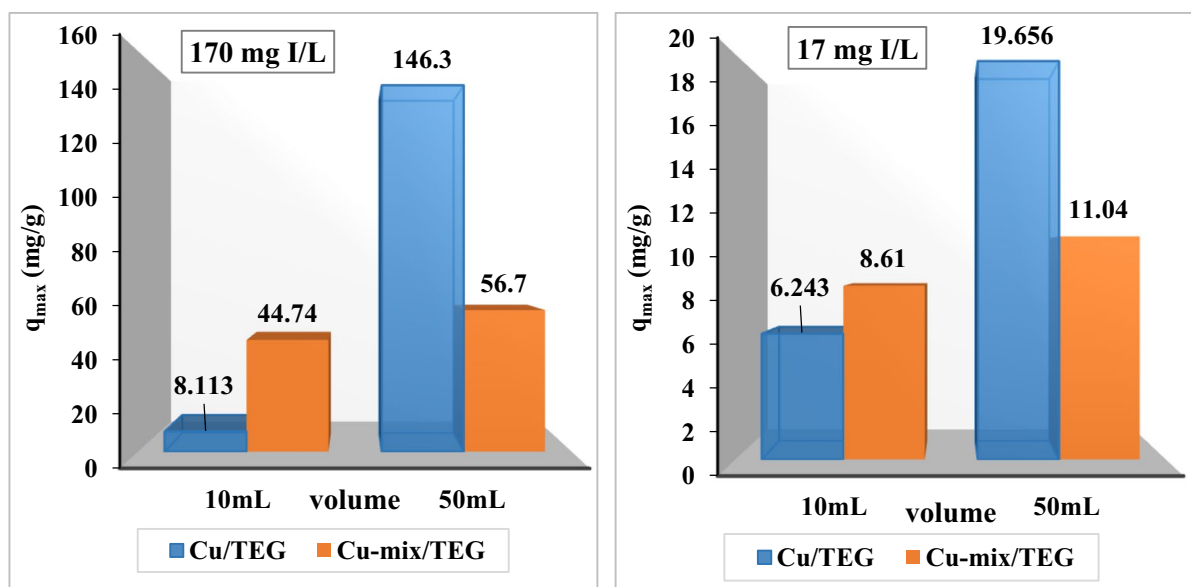


Fig. 6 Iodide adsorption tests onto Cu/TEG and Cu-mix/TEG (sorbent mass: 10 mg)

Fig. 7 Sorption of chromium on Cu/TEG, as a function of time and temperature (10 mg·L⁻¹, pH 7)

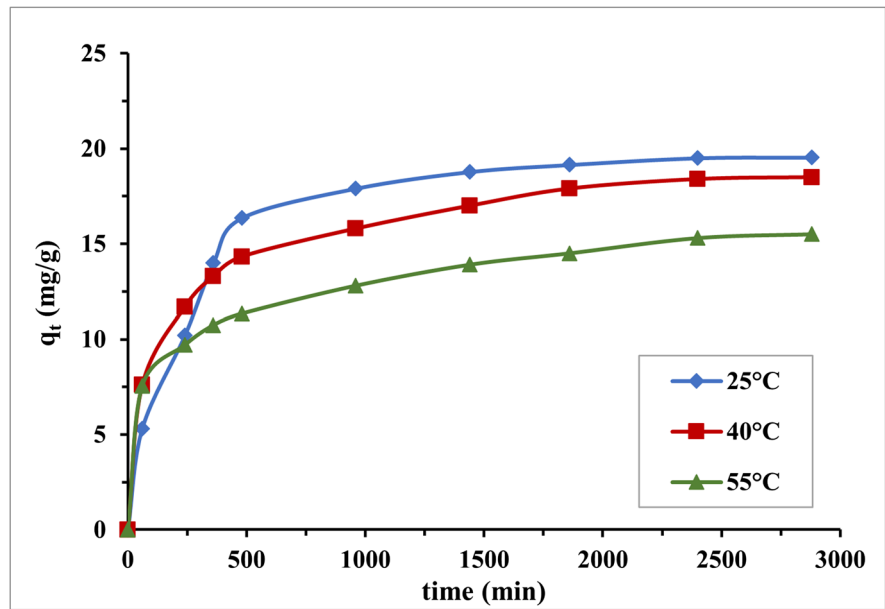


Table 3 Parameters of the kinetic equations in different temperatures

Models	Parameters	25 °C	40 °C	55 °C
Pseudo-first order	k_1	$1.9 \cdot 10^{-3}$	$1.6 \cdot 10^{-3}$	$0.4 \cdot 10^{-3}$
	q_e	11.9	11.1	9.5
	R^2	0.9827	0.9848	0.9581
Pseudo-second order	k_2	$2.65 \cdot 10^{-4}$	$3.20 \cdot 10^{-4}$	$3.52 \cdot 10^{-4}$
	q_e	20.9	19.4	16.2
	R^2	0.9990	0.9986	0.9967
Elovich	α	0.332	0.753	0.981
	β	0.264	0.350	0.467
	R^2	0.9569	0.9936	0.9902
Intraparticle	k_{int-1}	0.7392	0.692	0.626
	R^2	0.9926	0.9704	0.9062
	k_{int-2}	0.100	0.138	0.141
	R^2	0.9175	0.9646	0.9861

The calculated thermodynamic parameters are given in Table 4. The negative values of the Gibbs free energy change reflect the spontaneity of the process in all temperatures studied. The fact that the enthalpy change, ΔH^0 , is negative implies that the adsorption reaction is exothermic in nature. The positive ΔS^0 value indicates the increased randomness at the solid-solution interface during chromium sorption.

Table 4 Thermodynamic data of chromium sorption on Cu/TEG

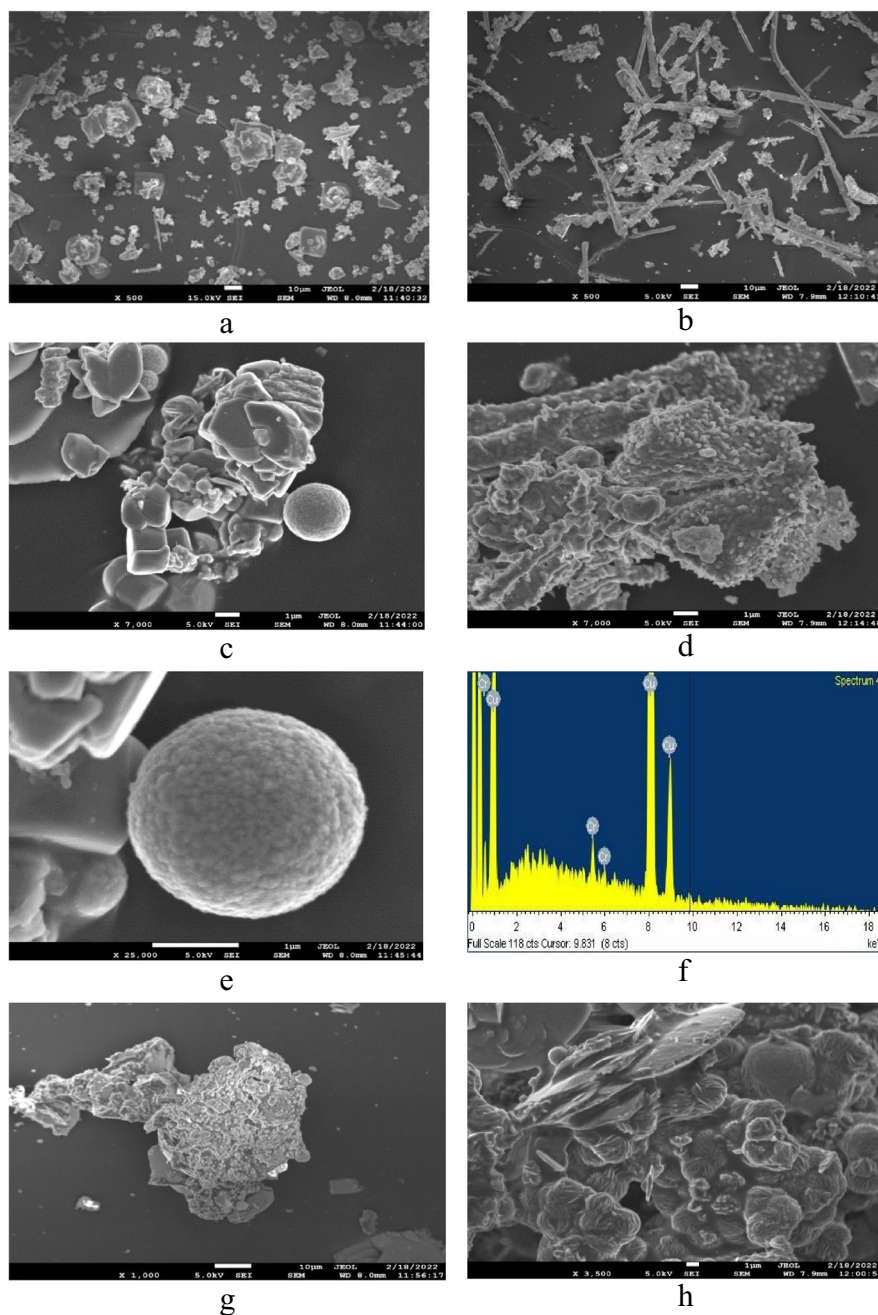
T (°C)	ΔH^0 (kJ/mol)	ΔS^0 (kJ/mol)	ΔG^0 (kJ/mol)
25	-11.3	0.026	-18.9
35			-19.2
45			-19.4
55			-19.7

3.3 Characterization of Adsorbents After Adsorption

3.3.1 SEM Study

The morphology of the Cu/TEG is shown in the following SEM images (Fig. 8a, c, and e). The nanoparticles appear to have good dispersion and uniform shape with composition of 98.5% copper. The corresponding images after adsorption of chromium (10 mg·L⁻¹) are given in Fig. 8b and d along with the EDS spectrum (Fig. 8f) which shows the elemental analysis on the loaded NPs and the Cr-peak well observed. In these images, the nanoparticles appear to form agglomerates and their composition determined to be 77.8% copper and 32.2% chromium. In Figs. 8g and 7h, the SEM images of the Cu-mix/TEG are illustrated before and after the Cr

Fig. 8 SEM–EDS photos of Cu/TEG nanoparticles after their interaction for 24 h with chromium solution concentration $10 \text{ mg}\cdot\text{L}^{-1}$, pH 7



sorption where agglomerations and dense structure can be observed.

3.3.2 FTIR Study

The FTIR spectra of the Cu/TEG before and after Cr sorption are given in Fig. 9. The peaks at 2920 and 2850 cm^{-1} corresponding to the asymmetric

(vas) and symmetric (vs) vibrations of the methylene groups ($-\text{CH}_2$) appear the same after the sorption, while broadening of the band around 3400 cm^{-1} indicates interaction of chromium with hydroxyl groups. The shift and change of the peaks at 1626 and 1382 cm^{-1} indicate that chromium interacts with hydrogen bonds and C-O bond of the ethers. As a result of the oxidation of Cu-NPs, the

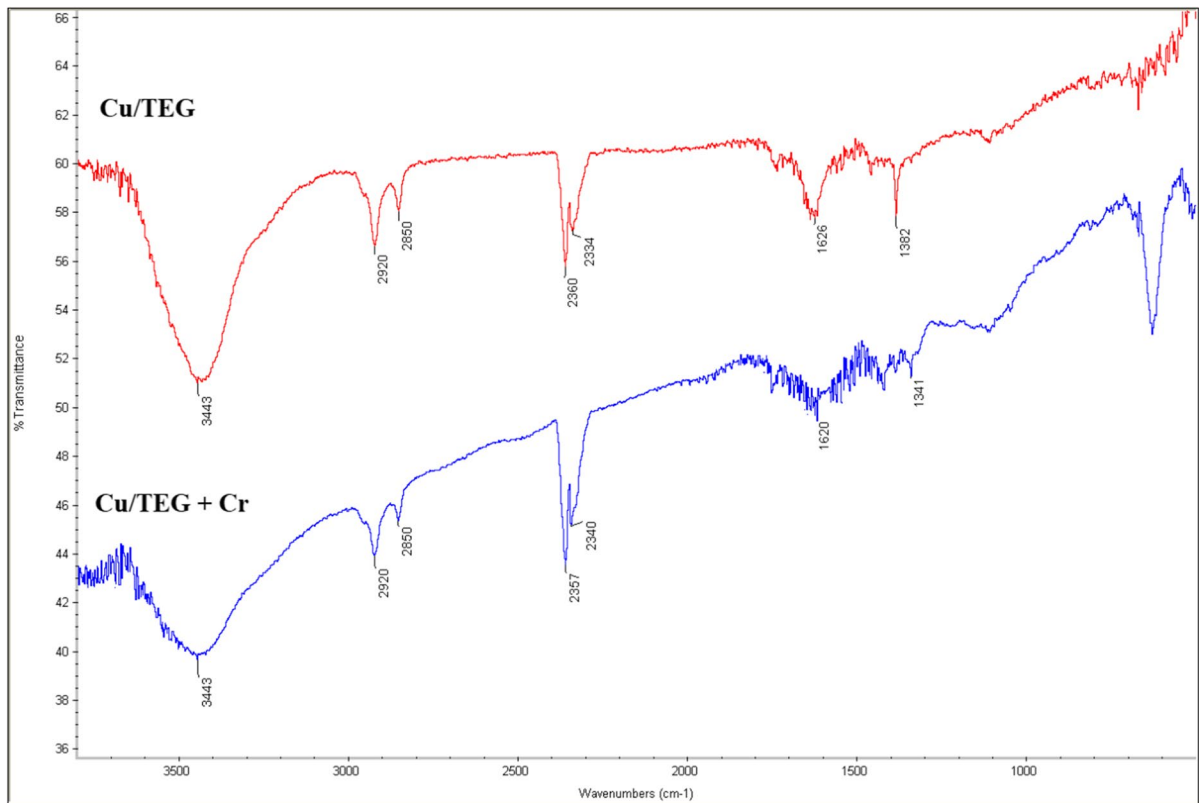


Fig. 9 FTIR spectra of Cu/TEG nanoparticles before and after Cr sorption

peak near 620 cm^{-1} corresponding to Cu–O was observed.

3.3.3 X-ray Photoelectron Spectroscopy

The XPS spectra of the Cu nanoparticles after the adsorption of chromium were examined to obtain information about the mechanism of the Cr removal by the nanoparticles. Figure 10 presents the Cu-2*p* (Fig. 10a) and Cr-2*p* (Fig. 10b) core-level spectra of the Cu nanoparticles after the Cr adsorption. The Cu nanoparticles (Fig. 10a) are partially oxidized, which is confirmed by the Cu(II) oxide and Cu(II) hydroxide peaks at 933.76 and 934.67 eV, respectively, while the presence of “shake-up” satellite peaks confirms the existence of oxide [Biesinger, 2017; Biesinger et al., 2010]. Detailed analysis in Cr-2*p* peak (Fig. 10b) shows that the peak structure can be deconvoluted into three components at 587.1, 576, and 569 eV attributed to the Cr-2*p*_{1/2}, Cr-2*p*_{3/2}, and Cu-LMM Auger peak, respectively. Unfortunately, the

Cu-LMM peak appears into the range of Cr-2*p* core-level spectrum due to overlap from Cu nanoparticles. The Cr-2*p*_{3/2} appears at binding energies ~576 eV attributed to Cr(III) oxide [Biesinger et al., 2004; Wright & Barron, 2017]. These findings indicate that the dominating process is based on Cr(VI) reduction, followed by simultaneous Cu oxidation, implying that the rate-controlling step is based on redox reactions [Ho et al., 2001].

Therefore, our findings revealed a complicated adsorption which proceeds by more than one mechanism. The electrostatic attractions between Cr(VI) ions and positively charged sorbent surface (Cu/TEG) lead to chemical sorption by sharing or replacing electrons between reactive sites on sorbent and sorbate (1st step). The 2nd step is explained as the reduction of Cr(VI) under the existence of Cu⁰ followed by intraparticle diffusion which seems to be the rate-controlling step.

Concerning the Cu-mix/TEG, the Cr adsorption is not favored because of the dominated negative

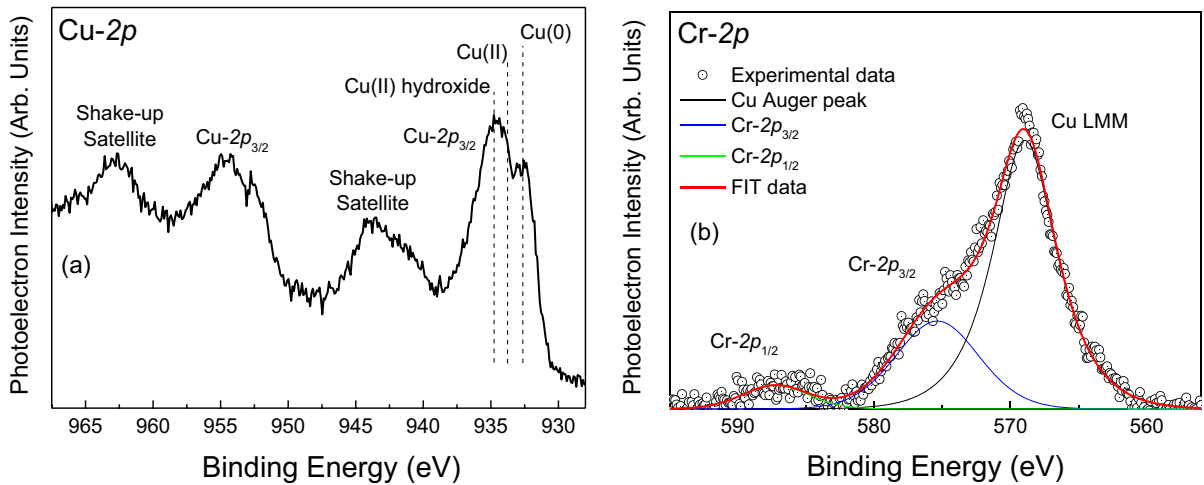


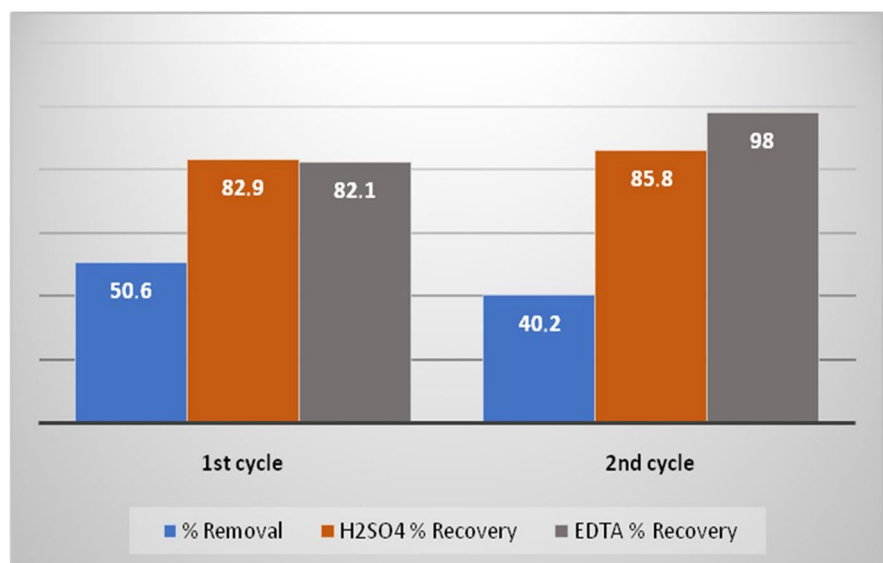
Fig. 10 XPS spectra of the Cu/TEG sample after Cr sorption: a Cu-2p core-level spectrum and b Cr-2p core-level spectrum

charge on the NPs surface, whereas ion exchange is taking place in this case. Redox reactions can also not occur since the nanoparticles are consisted of Cu compounds, and hence, this sorbent exhibited lower sorption capacity especially at high Cr concentrations. Similar Cu-ox/PEG NPs due to the cooper oxidation whereas in the case of Cu/PEG, the low sorption capacity can be explained by the type of the organic coating and the degree of coverage (60% PEG) which seem to hinder the approach of Cr ions to the NPs surface.

3.4 Regeneration Experiments

After the end of the adsorption experiments, the adsorbent Cu/TEG was subjected to regeneration testing to determine its reusability. The histogram in Fig. 11 shows the rates of chromium removal and subsequent recovery with EDTA and H₂SO₄. It is observed that the recovery of chromium after two loading cycles exceeds 80% and especially in the case of regeneration with EDTA is almost total (98%). These results are of great importance as it confirms the possibility of reusing Cu/TEG

Fig. 11 Adsorption and recovery tests of chromium with Cu/TEG material



material, which implies both material savings and cost reduction of the whole process.

4 Conclusions

The Cr removal from water was investigated using Cu-based nanoparticles in the concentration range 0.25–15 mg/L. The formation of different nanoparticles depends on the conditions of synthesis and the organic coating used, which influences the adsorption capacity of the materials through different adsorption mechanisms.

Metallic Cu-NPs coated with TEG exhibited significant sorption capacity lowering the equilibrium Cr concentration below the acceptable limit of 50 mg·L⁻¹ in aqueous solutions as well as in simulated water. The adsorption was better adjusted to the Langmuir equation with a maximum uptake capacity of 3.4 mg·g⁻¹ at the initial concentration C_{in} 1.0 mg·L⁻¹.

The kinetic studies showed that the adsorption was impacted by more than one mechanism, mainly chemisorption, and described by different kinetic models including the pseudo-second-order rate model, Elovich, and intraparticle diffusion model.

The Cu-NPs are promising agents in water treatment technology regarding their biocompatibility, stability, good uptake capacity, and reusability.

It is shown that the structure, the type, and the degree of coverage/organic coating of the Cu-based NPs affect their interaction with chromium in solutions and the Cr removal mechanism which is governed by electrostatic interactions and redox reactions, or ion exchange.

Acknowledgements The groups of NPs laboratory as well as of XPS laboratory of the Aristotle University of Thessaloniki are thankfully acknowledged.

Funding Open access funding provided by HEAL-Link Greece.

Data Availability The datasets generated during and/or analyzed during the current study are available from the corresponding author on reasonable request.

Declarations

Competing Interests The authors declare no competing interests.

Open Access This article is licensed under a Creative Commons Attribution 4.0 International License, which permits use, sharing, adaptation, distribution and reproduction in any medium or format, as long as you give appropriate credit to the original author(s) and the source, provide a link to the Creative Commons licence, and indicate if changes were made. The images or other third party material in this article are included in the article's Creative Commons licence, unless indicated otherwise in a credit line to the material. If material is not included in the article's Creative Commons licence and your intended use is not permitted by statutory regulation or exceeds the permitted use, you will need to obtain permission directly from the copyright holder. To view a copy of this licence, visit <http://creativecommons.org/licenses/by/4.0/>.

References

- Abuzalat, O., Tantawy, H., Mokhtar, M., & Baraka, A. (2020). Nano-porous bimetallic organic frameworks (Fe/Co)-BDC, a breathing MOF for rapid and capacitive removal of Cr-oxyanions from water. *Journal of Water Process Engineering*, *46*, 102537. <https://doi.org/10.1016/j.jwpe.2021.102537>
- Acharya, R., Lenka, A., Parida, K. (2021). Magnetite modified amino group based polymer nanocomposites towards efficient adsorptive detoxification of aqueous Cr (VI): A review *Journal of Molecular Liquids* 337 <https://doi.org/10.1016/j.molliq.2021.116487>
- Antonoglou, O., & Dendrinou-Samara, C. (2021). Polyols as a toolbox for the preparation of inorganic-based nanostructures. *RSC Nanoscience and Nanotechnology*, *50*, 51–72. <https://doi.org/10.1039/9781839163623-00051>
- Bampaiti, A., Noli, F., & Misaelides, P. (2013). Investigation of the Cr(VI) removal from aqueous solutions by stabilized iron-nanoparticles using ⁵¹Cr-tracer. *Journal of Radioanalytical and Nuclear Chemistry*, *298*, 909–914. <https://doi.org/10.1007/s10967-013-2483-1>
- Biesinger, M. C. (2017). Advanced analysis of copper X-ray photoelectron spectra. *Surface and Interface Analysis*, *49*, 1325–1334. <https://doi.org/10.1002/sia.6239>
- Biesinger, M. C., Brown, C., Mycroft, J. R., Davidson, R. D., & McIntyre, N. S. (2004). X-ray photoelectron spectroscopy studies of chromium compounds. *Surface and Interface Analysis*, *36*(12), 1550–1563. <https://doi.org/10.1002/sia.1983>
- Biesinger, M. C., Lau, L. W. M., Gerson, A. R., Smart, R., & St, C. (2010). Resolving surface chemical states in XPS analysis of first row transition metals, oxides, and hydroxides: Sc, Ti, V, Cu and Zn. *Applied Surface Science*, *257*(3), 887–898. <https://doi.org/10.1016/j.apsusc.2010.07.086>
- Chandra, C., & Khan, F. (2020). Nano-scale zerovalent copper: Green synthesis, characterization and efficient removal of uranium. *Journal of Radioanalytical and Nuclear Chemistry*, *324*, 589–597. <https://doi.org/10.1007/s10967-020-07080-1>
- Cheung, W. H., Szeto, Y. S., & McKay, G. (2007). Intraparticle diffusion processes during acid dye adsorption onto chitosan. *Bioresource Technology*, *98*(15), 2897–2904. <https://doi.org/10.1016/j.biortech.2006.09.045>

- Des Marias, T. L., & Costa, M. (2019). Mechanisms of chromium-induced toxicity. *Current Opinion in Toxicology*, 14, 1–7. <https://doi.org/10.1016/j.cotox.2019.05.003>
- Farooqi, Z. H., Akram, M. W., Begum, R., Wu, W., & Irfan, A. (2021). Inorganic nanoparticles for reduction of hexavalent chromium: Physicochemical aspects. *Journal of Hazardous Materials*, 402, 123535. <https://doi.org/10.1016/j.jhazmat.2020.123535>
- Freundlich, H. F. (1906). Adsorption in solution. *Physics, Chemistry and Society*, 40, 1361–1368.
- Gautam, A., Rawat, S., Verma, L., Singh, J., Sikarwar, S., Yadav, B. C., & Kalamdhad, A. S. (2018). Green synthesis of iron nanoparticle from extract of waste tea: An application for phenol red removal from aqueous solution. *Environmental Nanotechnology, Monitoring & Management*, 10, 377–387. <https://doi.org/10.1016/j.enmm.2018.08.003>
- Giannousi, K., Lafazanis, K., Arvanitidis, J., Pantazaki, A., & Dendrinou-Samara, C. (2014). Hydrothermal synthesis of copper based nanoparticles: Antimicrobial screening and interaction with DNA. *Journal of Inorganic Biochemistry*, 133, 24–32. <https://doi.org/10.1016/j.jinorgbio.2013.12.009>
- Giannousi, K., Hatzivassiliou, E., Mourdikoudis, S., Pantazaki, A., & Dendrinou-Samara, C. (2016). Synthesis and biological evaluation of PEGylated CuO nanoparticles. *Journal of Inorganic Biochemistry*, 164, 82–90. <https://doi.org/10.1016/j.jinorgbio.2016.09.003>
- Gkanatsiou, C., Karamanoli, K., Menkissoglu-Spirodi, U., & Dendrinou-Samara, C. (2019). Composition effect of Cu-based nanoparticles on phytopathogenic bacteria. *Antibacterial Studies and Phytotoxicity Evaluation, Polyhedron*, 170, 395–403. <https://doi.org/10.1016/j.poly.2019.06.002>
- Gözetten, I., & Tunç, M. (2022). Palladium nanoparticles supported on activated carbon (C) for the catalytic hexavalent chromium reduction. *Water, Air, and Soil Pollution*, 233(4), 1–14. <https://doi.org/10.1007/s11270-021-05479-4>
- Gupta, V. K., Chandra, R., Tyagi, I., & Verma, M. (2016). Removal of hexavalent chromium ions using CuO nanoparticles for water purification applications. *Journal of Colloid and Interface Science*, 478, 54–62. <https://doi.org/10.1016/j.jcis.2016.05.064>
- Ho, Y. S., Chiang, C. C., & Hsu, Y. C. (2001). Sorption kinetics for dye removal from aqueous solution using activated clay. *Separation Science and Technology*, 36(11), 2473–2488. <https://doi.org/10.1081/SS-100106104>
- Jawed, A., Saxena, V., & Pandey, L. M. (2020). Engineered nanomaterials and their surface functionalization for the removal of heavy metals: A review. *Journal of Water Process Engineering*, 33, 101009. <https://doi.org/10.1016/j.jwpe.2019.101009>
- Jiang, B., Gong, Y., Gao, J., Sun, T., Liu, Y., Oturan, N., & Oturan, M. (2019). The reduction of Cr(VI) to Cr(III) mediated by environmentally relevant carboxylic acids: State-of-the-art and perspectives, Review. *Journal of Hazardous Materials*, 365, 205–226. <https://doi.org/10.1016/j.jhazmat.2018.10.070>
- Kaprara, E., Seridou, P., Tsiamilis, V., Mitrakas, M., Vourlias, G., Tsiaoussis, I., Kaimakamis, G., Pavlidou, E., Andritsos, N., & Simeonidis, K. (2013). Cu-Zn powders as potential Cr(VI) adsorbents for drinking water. *Journal of Hazardous Materials*, 262, 606–613.
- Kaprara, E., Tziarou, N., Kalaitzidou, K., Simeonidis, K., Balcells, L., Pannunzio, E. V., Zouboulis, A., & Mitrakas, M. (2017). The use of Sn (II) oxy-hydroxides for the effective removal of Cr (VI) from water: Optimization of synthesis parameters. *Science of the Total Environment*, 605, 190–198. <https://doi.org/10.1016/j.scitotenv.2017.06.199>
- Khani, R., Roostaei, B., Bagherzade, G., & Moudi, M. (2018). Green synthesis of copper nanoparticles by fruit extract of *Ziziphus spina-christi* (L.) Willd: Application for adsorption of triphenylmethane dye and antibacterial assay. *Journal of Molecular Liquids*, 255, 541–549. <https://doi.org/10.1016/j.molliq.2018.02.010>
- Langmuir, I. (1916). The constitution and fundamental properties of solids and liquids. *Journal of the American Chemical Society*, 38, 2221–2295.
- Lima, E.C., Adebayo, M.A., Machado, F.M. (2015). Chapter 3-Kinetic and equilibrium models of adsorption. In: *Carbon nanomaterials as adsorbents for environmental and biological applications*, Bergmann, C.P., Machado, F.M. editors, ISBN 978–3–319–18874–4, Springer 33–69. https://doi.org/10.1007/978-3-319-18875-1_3.
- Liu, B. (2012). One-dimensional copper hydroxide nitrate nanorods and nanobelts for radiochemical applications. *Nanoscale*, 4, 7194–7198. <https://doi.org/10.1039/C2NR32439C>
- Liu, Y., & Liu, Y. J. (2008). Biosorption isotherms, kinetics and thermodynamics. *Separation and Purification Technology*, 61(3), 229–242. <https://doi.org/10.1016/j.seppur.2007.10.002>
- Mohamed, A. A., Ismail, E. M., & Ali, S. (2020). Ultrasensitive catalytic assessment of chromium(VI) using digital imaging. *Microchemical Journal*, 157, 105054. <https://doi.org/10.1016/j.microc.2020.105054>
- Mortazavian, S., An, H., Chun, D., & Moon, J. (2018). Activated carbon impregnated by zero-valent iron nanoparticles (AC/nZVI) optimized for simultaneous adsorption and reduction of aqueous hexavalent chromium: Material characterizations and kinetic studies. *Chemical Engineering Journal*, 353, 781–795. <https://doi.org/10.1016/j.cej.2018.07.170>
- Poul, L., Ammar, S., Jouini, N., & Fievet, F. (2003). Synthesis of inorganic compounds (metal, oxide and hydroxide) in polyol medium: A versatile route related to the sol-gel process. *Journal of Sol-Gel Science and Technology*, 26, 261–265. <https://doi.org/10.1023/A:1020763402390>
- Prasad, S., Yadav, K. K., Kumar, S., Gupta, N., Cabral-Pinto, M. M. S., Rezania, S., Radwan, N., & Alam, J. (2021). Chromium contamination and effect on environmental health and its remediation: A sustainable approaches. *Journal of Environmental Management*, 285, 112174. <https://doi.org/10.1016/j.jenvman.2021.112174>
- Prasetyo, L., Do, D. D., & Nicholson, D. (2018). A coherent definition of Henry constant and isosteric heat at zero loading for adsorption in solids – An absolute accessible volume. *Chemical Engineering Journal*, 334, 143–152. <https://doi.org/10.1016/j.cej.2017.10.022>
- Puigdomènech, I., INPUT, SED, And PREDOM: Computer programs drawing equilibrium diagrams, Report TRITA-OOK-3010, Royal Institute of Technology (KTH), Dept.

- Inorg. Chemistry, Stockholm, 1983. MEDUSA (Make Equilibrium Diagrams Using Sophisticated Algorithms).
- Sahoo, S. K., Panigrahi, G. K., Sahoo, J. K., Pradhan, A. K., Purohit, A. K., & Dhal, J. P. (2021). Electrospun magnetic polyacrylonitrile-GO hybrid nanofibers for removing Cr(VI) from water. *Journal of Molecular Liquids*, 326, 115364. <https://doi.org/10.1016/j.molliq.2021.115364>
- Seridou, P., Tsiamili, V., Mitrakas, M., Vourlias, G., Tsiaousis, I., Kaimakamis, G., Pavlidou, E., Andritsos, N., & Simeonidis, K. (2013). Cu-Zn powders as potential Cr(VI) adsorbents for drinking water. *Journal of Hazardous Materials*, 262, 606–613. <https://doi.org/10.1016/j.jhazmat.2013.09.039>
- Sharma, N., Sodhi, K.K., Kumar, M., Singh, D.K. (2021). Heavy metal pollution: Insights into chromium eco-toxicity and recent advancement in its remediation, Environment Nanotechnology Monitoring and Management 15 <https://doi.org/10.1016/j.enmm.2020.100388>
- Simeonidis, K., Kaprara, E., Samaras, T., Angelakeris, M., Pliatsikas, N., Vourlias, G., Mitrakas, M., & Andritsos, N. (2015). Optimizing magnetic nanoparticles for drinking water technology: The case of Cr(VI). *Science of the Total Environment*, 535, 61–68. <https://doi.org/10.1016/j.scitotenv.2015.04.033>
- Sing, K. S. (1985). Reporting physisorption data for gas/solid systems with special reference to the determination of surface area and porosity. *Pure and Applied Chemistry*, 57(4), 603–619. <https://doi.org/10.1351/pac198557040603>
- Vagheti, J. C. P., Lima, E. C., Royer, B., da Cunha, B. M., Cardoso, N. F., Brasil, J. L., & Dias, S. L. P. (2009). Pecan nutshell as biosorbent to remove Cu(II), Mn(II) and Pb(II) from aqueous solutions. *Journal of Hazardous Materials*, 162(1), 270–280. <https://doi.org/10.1016/j.jhazmat.2008.05.039>
- Wadhawana, S., Jaina, A., Nayyara, J., & Kumar Mehta, S. (2020). Role of nanomaterials as adsorbents in heavy metal ion removal from wastewater: A review. *Journal of Water Process Engineering*, 33, 101038.
- Wright, K. D., & Barron, A. R. (2017). Catalyst residue and oxygen species inhibition of the formation of hexahapto-metal complexes of group 6 metals on single-walled carbon nanotubes. *Journal of Carbon Research*, 3(2), 17. <https://doi.org/10.3390/c3020017>
- Yi, Y., Lv, J., Liu, Y., & Wu, G. (2017). Synthesis and application of modified Litchi peel for removal of hexavalent chromium from aqueous solutions. *Journal of Molecular Liquids*, 225, 28–33. <https://doi.org/10.1016/j.molliq.2016.10.140>
- Zarrabi, A., & Ghasemi-Fasaei, R. (2021). Preparation of green synthesized copper oxide nanoparticles for efficient removal of lead from wastewaters. *International Journal of Phytoremediation*, 6, 1–12. <https://doi.org/10.1080/15226514.2021.1984385>
- Zhang, H., Tian, Y., Niu, Y., Dong, X., Lou, H., & Zhou, H. (2022). Lignosulfonate/N-butylaniline hollow microspheres for the removal of Cr(VI): Fabrication, adsorption isotherm and kinetics. *Journal of Water Process Engineering*, 46, 102588. <https://doi.org/10.1016/j.jwpe.2022.102588>
- Zhu, Y., Jin, Y., Chang, K., Chen, Z., Li, X., Wu, X., Jin, C., Ye, F., Shen, R., Dong, W., Asiri, A. M., Marwani, H. M., & Sheng, G. (2018). Use of molybdenum disulfide nanosheets embellished nanoiron for effective capture of chromium (VI) ions from aqueous solution. *Journal of Molecular Liquids*, 259, 376–383. <https://doi.org/10.1016/j.molliq.2018.03.050>

Publisher's Note Springer Nature remains neutral with regard to jurisdictional claims in published maps and institutional affiliations.